



Contents lists available at ScienceDirect

Physics of the Earth and Planetary Interiors

journal homepage: www.elsevier.com/locate/pepi

Transmission electron microscopy characterization of dislocations and slip systems in K-lingunite: Implications for the seismic anisotropy of subducted crust

A. Mussi^{a,*}, P. Cordier^{a,c}, D. Mainprice^b, D.J. Frost^c^a Unité Matériaux et Transformations, UMR 8207 CNRS-Université Lille 1, Université Lille Nord de France, F-59655 Villeneuve d'Ascq, France^b Géosciences Montpellier, UMR CNRS 5243, Université Montpellier 2, Place Eugène Bataillon, 34095 Montpellier Cedex 5, France^c Bayerisches Geoinstitut, Universität Bayreuth, Germany

ARTICLE INFO

Article history:

Received 26 March 2010

Received in revised form 7 June 2010

Accepted 21 June 2010

Edited by: K. Hirose.

Keywords:

K-lingunite

Dislocation

Slip systems

Crystal preferred orientations

Seismic properties

ABSTRACT

In order to estimate the seismic anisotropy of subducted crust, polycrystalline samples of KAlSi_3O_8 K-lingunite (25% of the total subducted transformed sediments), have been synthesized and deformed under the temperature and pressure conditions of the subducted slabs. Transmission electron microscopy (TEM) characterizations of the recovered samples reveal that the microstructures are clearly dominated by $[001]$ glide involving screw dislocations. For this reason, only $\{100\}$ could be identified as glide planes, the question of $[001]$ slip on $\{110\}$ remains open. Few $1/2\langle 111 \rangle$ dislocations were observed gliding on $\{110\}$ planes, which implies that $1/2\langle 111 \rangle\{110\}$ is a harder slip system than those involving $[001]$ slip. The occurrence of sub-grain boundaries suggests that diffusion and climb might be active under these conditions.

To assess the texture of polycrystalline K-lingunite, the crystal preferred orientations (CPOs) were calculated using visco-plastic self-consistent (VPSC) polycrystalline plasticity model in simple shear using the slip systems identified by TEM. Finally, the seismic properties of K-lingunite aggregates were calculated from the CPO and single crystal elasticity tensor. K-lingunite is predicted to have a high seismic anisotropy, which could combine constructively with one of the stishovite (same proportion as K-lingunite at the transition zone depth ranges).

© 2010 Elsevier B.V. All rights reserved.

1. Introduction

The fate of subducted oceanic and continental crust in the mantle is of primary importance for the dynamics of the Earth. It depends largely on the rheological properties of the materials composing the slabs. The high-pressure behaviour of feldspars deserves attention since these minerals are a major component of the continental crust and since they host potassium, an important heat producing radionuclide. At ca. 9 GPa, KAlSi_3O_8 orthoclase transforms to a tetragonal polymorph with a hollandite structure (hereafter referred to as K-lingunite since the hollandite structured $\text{NaAlSi}_3\text{O}_8$ has been previously named lingunite by Liu and El Goresy (2007)). The first synthesis and determination of the crystal structure of K-lingunite ($I4/m$) was conducted by Ringwood et al. (1967). Yagi et al. (1994) and Urakawa et al. (1994) have further investigated its stability using in situ X-ray diffraction and quench experiments. At higher pressure (ca. 20 GPa), K-lingunite transforms to an unquenchable monoclinic $I2/m$ crystal structure at about 20 GPa (Ferroir et al., 2006). Natural K-lingunite, has been

identified in shock veins of heavily deformed ordinary chondrites (Gillet et al., 2000; Tomioka et al., 2000; Xie et al., 2001) and in the SNC achondrite Zagami (Langenhorst and Poirier, 2000a,b). Terrestrial silicate hollandite has also been reported in a strongly shocked anorthosite from the central uplift of the Manicouagan impact crater, Canada (Langenhorst & Dressler, 2003).

Assessment of K-lingunite in subducted slabs requires the knowledge of the equation of state and elastic properties of this phase as a function of pressure. Zhang et al. (1993) have determined the compression behaviour of K-lingunite single crystals from ambient pressure up to 4.5 GPa. These results have been extended to higher pressure (15–27 GPa) by Nishiyama et al. (2005). More recently, Mookherjee and Steinle-Neumann (2009) have calculated the elastic properties of K-lingunite up to 100 GPa, based on the density functional theory. To date there is no data of plastic deformation of polycrystals of K-lingunite. However, the single crystal elastic properties cannot be transferred directly to the scale of the polycrystalline aggregate without knowing the crystal preferred orientations (CPOs). Plastic deformation by dislocation glide is one of the most efficient mechanisms to generate strong CPO. In this work, transmission electron microscopy (TEM) characterizations of K-lingunite specimens deformed at high pressure are performed to identify the deformation mechanisms of this phase.

* Corresponding author. Tel.: +33 0 320 43 49 60; fax: +33 0 320 43 65 91.
E-mail address: alexandre.mussi@univ-lille1.fr (A. Mussi).

This information is used to model the CPO and the seismic properties of textured K-lingunite aggregates.

2. Material and experimental procedure

2.1. High-pressure preparation and deformation of the samples

K-lingunite was synthesized from a KAlSi_3O_8 glass in a multi-anvil press at 17 GPa and at temperatures ranging from 1400 to 1600 °C. After synthesis in quasi-hydrostatic conditions, the high-pressure phase was recovered and placed in another high-pressure cell designed to induce deviatoric stresses during the compression (Cordier and Rubie, 2001), at 1300 °C, with the same pressure. The deformation conditions corresponding to this second run were 17 GPa, 1300 °C for 1 h (sample 3753) and 1 h and a half (sample 2482). In this kind of experiments, large stresses applied during compression are relaxed at high temperature under pressure. After the run, the sample is quenched to ca. 100 °C in a few seconds before the slow release of pressure.

2.2. Transmission electron microscopy

Two doubly polished thin foils were obtained from each high-pressure cell. They were thinned to electron transparency with a Gatan® DuoMill™ Model 600 ion milling device and lightly carbon coated. TEM investigations have been performed at a 300 kV accelerating voltage with a Philips® CM30 microscope. As K-lingunite amorphises extremely rapidly under the electron beam damage, a Gatan® cold stage (liquid nitrogen temperature), a small condenser aperture (100 μm) and a small spot size (300 nm), were used in order to preserve the sample long enough to perform the defects characterization. With such an electron illumination, the incident beam current and the electron flux are respectively 14 nA and 1.2×10^8 electron $\text{nm}^{-2} \text{s}^{-1}$, which can be considered as low dose irradiation conditions.

The precession electron diffraction (PED) procedure was employed to orientate the grains and to select diffraction vectors. As this technique scans the incident beam in association with a transmitted beam de-scan, at a constant angle throughout the optic axis (Vincent and Midgley, 1994), the spot intensities are reasonably associated with the structure factor and the multiple diffractions are reduced. Indeed, from Morniroli and Ji (2009), the forbidden spots by screw axis and glide plane become very weak for low precession angles and disappear when precession angles reach 3° as in our case. Precession patterns are acquired with the “Spinning Star” device from the Nanomegas® Company. Dislocation Burgers vectors were characterized using the standard extinction conditions ($\mathbf{g} \cdot \mathbf{b} = 0$) as well as with the thickness fringe method (Ishida et al., 1980; Miyajima and Walte, 2009).

3. Visco-plastic self-consistent model and seismic properties

The visco-plastic self-consistent (VPSC) model has been established in Earth sciences by Wenk et al. (1991) as a model that provides a robust solution for the CPO development in mineral aggregates deforming by dislocation glide. The model was originally developed by Molinari et al. (1987) and extended to anisotropic materials by Lebensohn and Tomé (1993) and a recent review of the method is given by Tomé and Lebensohn (2004), thus only a short overview is presented in this section. This model has been successfully applied to many minerals of the Earth's mantle (e.g. olivine, Tommasi et al., 2000; wadsleyite, Tommasi et al., 2004; stishovite, Cordier et al., 2004).

The VPSC model is based on three assumptions: (i) the crystals that constitute the polycrystal deform uniquely by homogeneous intracrystalline slip, (ii) individual crystals obey a viscous rheology with shear strain rate proportional to shear stress raised to a power n , and (iii) the aggregate behaviour may be calculated as a volume average of the behaviour of the individual crystals. Locally, from crystal to crystal, stress and strain are heterogeneous and crystals, in an easy glide orientation, deform faster than those in low resolved shear stress orientations. Strain compatibility and stress equilibrium are ensured at the macroscopic scale, i.e. the polycrystalline stress (Σ_{ij}) and strain rate (E_{kl}) tensors are taken to be the volume average of the stress (σ_{ij}) and of the strain rates (ε_{kl}) tensors of the individual component crystals. The interaction between an individual crystal and a homogeneous effective medium (HEM) (i.e. the polycrystalline aggregate) is treated using the inclusion formalism of Eshelby (1957), where each crystal is considered as an ellipsoidal inclusion. Eshelby has shown that the ellipsoidal inclusion has the unique property of having uniform internal stress, strain and strain rate fields. The uniform stresses and strain rates of the individual crystals are thus related to the macroscopic HEM polycrystalline quantities through:

$$\varepsilon_{kl} - E_{kl} = -\alpha M_{ijkl}(\sigma_{ij} - \Sigma_{ij})$$

where M_{ijkl} is the interaction tensor which depends on the rheological properties of the polycrystal and the ellipsoidal shape of the inclusions. The constant α describes the interaction between crystals and the HEM, i.e. it imposes more or less stringent kinematics conditions on crystals. A zero value of α corresponds to Taylor (1938) model (the upper mechanical bound approach) that imposes a homogeneous strain on all crystals (i.e. $\varepsilon_{kl} = E_{kl}$) and requires that at least five independent slip systems are available. A value of one corresponds to the tangent VPSC model of Lebensohn and Tomé (1993), and an infinite value corresponds to the stress equilibrium model (i.e. the lower bound approach; Chastel et al., 1993). The VPSC and stress equilibrium models can operate with less than five independent slip systems, as locally strain compatibility is not required.

To perform a model calculation we need to define the initial CPO, the initial crystal shape, the interaction parameter α , the power law stress exponent (n), a constant imposed velocity gradient tensor, a set of slip systems and their relative critical resolved shear stresses. Here we have taken the initial CPO to be composed of 1000 random individual orientations with spherical shape. We have chosen the standard tangent model with $\alpha = 1$ for all simulations. We have no information about the stress exponent for K-lingunite from our experiments and we have assumed a value of 3, which is typical of many minerals at high temperature. The VPSC model is not very sensitive to n , between 3 and 5, and almost all minerals have stress exponents in this range. Increasing n rises the degree of CPO for a given finite strain. In the present models, an aggregate of 1000 random orientations was deformed with a constant velocity gradient tensor for simple shear for 80 identical steps of 0.025 equivalent strain, giving a final equivalent strain of 2.0 (shear strain $\gamma = 3.46$). The slip systems were determined by TEM, but we do not know their critical resolved shear stresses (CRSS). Based on the dislocation microstructure, we will propose the choice of CRSS.

4. Results

4.1. Dislocation observations and characterization

The specimen microstructure is heterogeneous. The grain size ranges from 45 to 85 μm and some are free of dislocations. Nevertheless, most of them contain dislocations generated by plastic deformation. The density of free dislocations has been estimated

Table 1
Reflecting planes \mathbf{g} and $\mathbf{g}\cdot\mathbf{b}$ product with Ishida's method.

\mathbf{g}	$\mathbf{g}\cdot\mathbf{b}$
$\bar{1}\ \bar{1}\ 0$	0
$4\ \bar{5}\ 1$	-1
$0\ \bar{3}\ 1$	-1

of the order of $3 \times 10^{12}\ \text{m}^{-2}$ using the method proposed by Ham (1961).

The samples show pervasive evidence of low-angle sub-grain boundaries (Fig. 1). In every image, the reflecting planes \mathbf{g} and the zone axis (ZA) are indicated. Typical dislocation microstructures of the K-lingunite are shown in Figs. 2 and 3. All the images in Fig. 2, are from the same area, but each of them was acquired with different diffracting conditions. The dislocation population of Fig. 2 is composed of two families: dislocations in sub-grain boundaries as well as free dislocations with $\rho \approx 3 \times 10^{12}\ \text{m}^{-2}$. Both families of dislocations are out of contrast with the diffraction vector $\mathbf{g} = \bar{1}\ \bar{1}\ 0$ (Fig. 2a). Moreover, following the method of Ishida et al. (1980), the value of the $\mathbf{g}\cdot\mathbf{b}$ product is $n = -1$ with $\mathbf{g} = 4\ \bar{5}\ 1$ (Fig. 2b) and $n = -1$ with $\mathbf{g} = 0\ \bar{3}\ 1$ (Fig. 2c). The analyses of the number of terminating fringes with Ishida's method are summarized in Table 1. Consequently, the Burgers vector of these dislocations is $[00\ \bar{1}]$.

The dislocations visible in Fig. 3 are in contrast with $\mathbf{g} = 2\ \bar{1}\ \bar{1}$, with a $\mathbf{g}\cdot\mathbf{b}$ product equal to $n = -1$ (Fig. 3a), and are standing end-on when viewed along $[00\ \bar{1}]$ (Fig. 3b). Considering other diffraction conditions, the Burgers vector of this family of dislocations is $[00\ \bar{1}]$ and they have a screw character. Determining the glide plane of

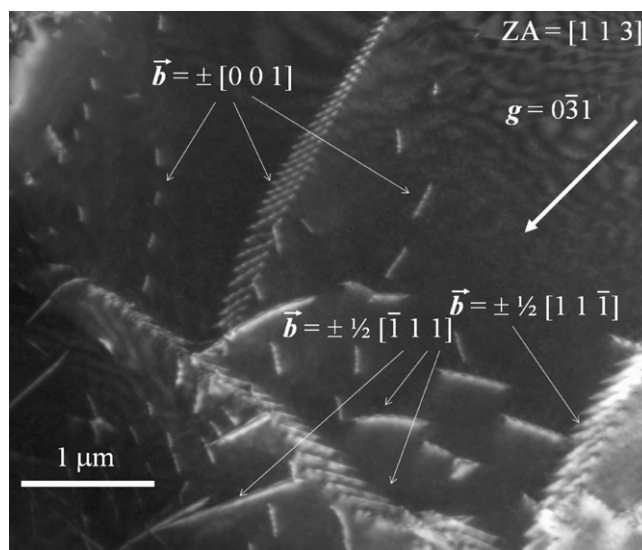


Fig. 1. Micrograph of sample 2482 in weak beam dark field (WBDF) condition ($\mathbf{g} = 0\ \bar{3}\ 1$), along the $[1\ 1\ 3]$ ZA. Four families of dislocations can be distinguished: $\pm[00\ \bar{1}]$ dislocations in sub-grain boundaries, $\pm[00\ \bar{1}]$ free dislocations, $1/2(1\ 1\ 1)$ dislocations in sub-grain boundaries and $1/2(1\ 1\ 1)$ free dislocations.

screw dislocations is difficult; however, Fig. 3b shows many $[00\ \bar{1}]$ screw dislocations aligned perpendicular to $[020]$ and to $[200]$. This observation suggests that $(0\ 1\ 0)$ and $(1\ 0\ 0)$ may be glide planes for $[00\ \bar{1}]$ dislocations.

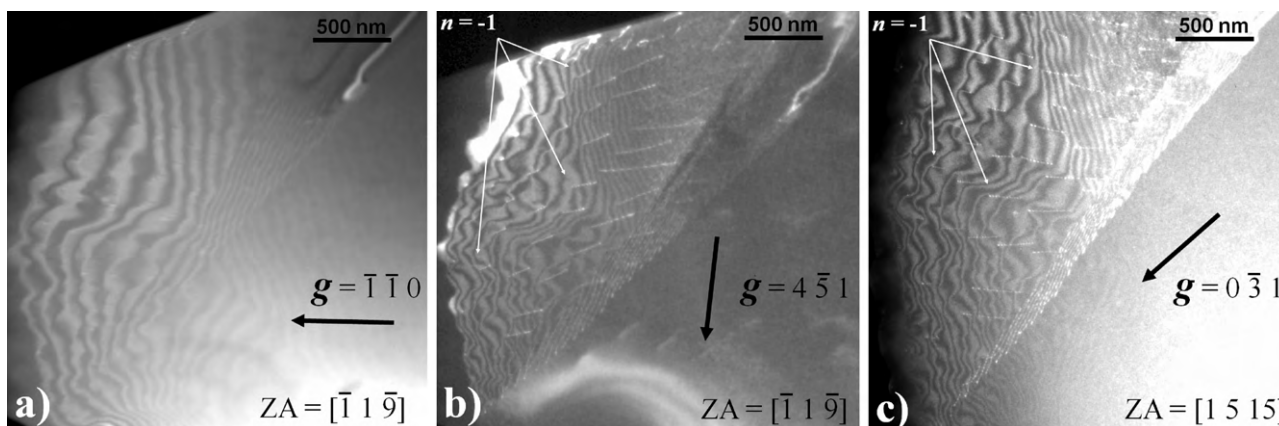


Fig. 2. Micrographs of sample 2482 in WBDF conditions showing only $[00\ \bar{1}]$ dislocations with two examples of determination of $n = \mathbf{g}\cdot\mathbf{b}$ using the thickness fringes method. (a) Condition $\mathbf{g} = \bar{1}\ \bar{1}\ 0$, along the $[\bar{1}\ 1\ \bar{9}]$ ZA; (b) condition $\mathbf{g} = 4\ \bar{5}\ 1$, along the $[\bar{1}\ 1\ \bar{9}]$ ZA; (c) condition $\mathbf{g} = 0\ \bar{3}\ 1$, along the $[1\ 5\ 15]$ ZA.

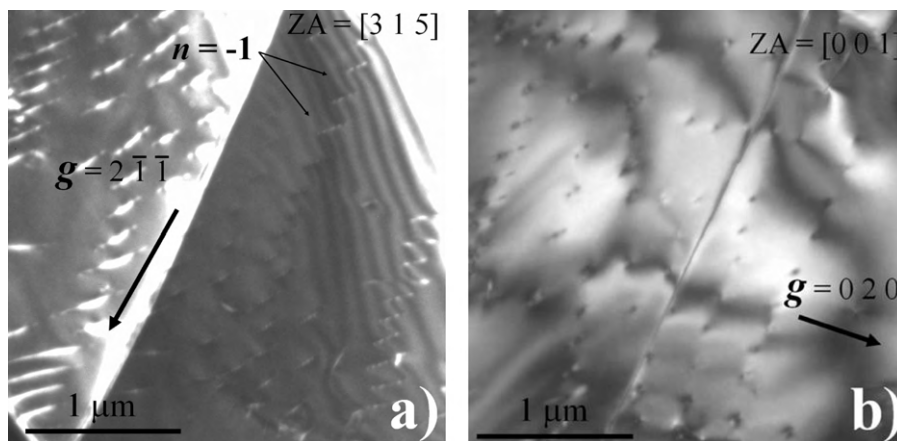


Fig. 3. WBDF pictures of sample 3753 obtained with $\mathbf{g} = 2\ \bar{1}\ \bar{1}$, along the $[3\ 1\ 5]$ ZA (a) and $\mathbf{g} = 0\ 2\ 0$, along the $[00\ \bar{1}]$ ZA (b). These micrographs show numerous $[00\ \bar{1}]$ dislocations with one example of determination of $n = \mathbf{g}\cdot\mathbf{b}$ using the thickness fringes method.

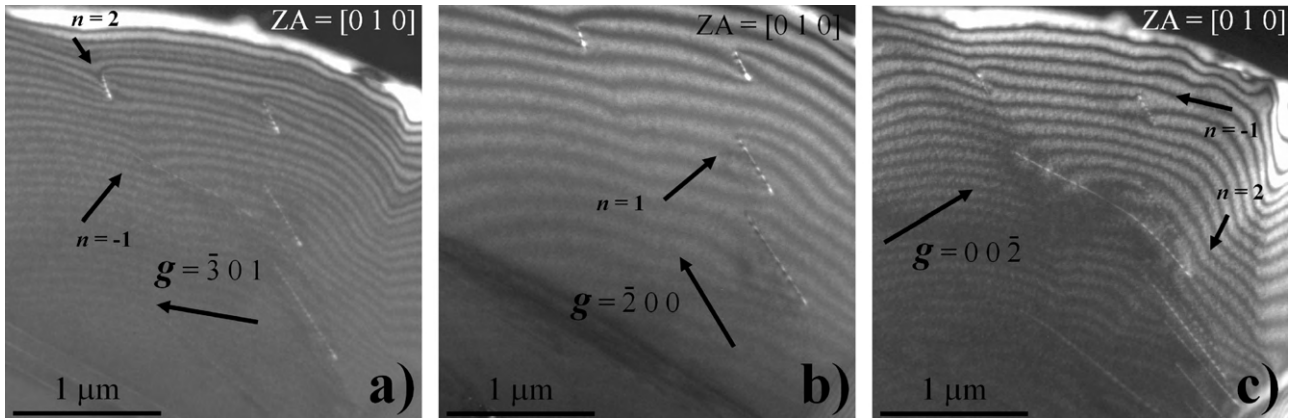


Fig. 4. WBDF images of sample 2482 with $g = \bar{3}01$, along the $[0\ 1\ 0]$ ZA (a); $g = \bar{2}00$, along the $[0\ 1\ 0]$ ZA (b) and $g = 00\bar{2}$, along the $[0\ 1\ 0]$ ZA (c). Micrographs revealing $1/2[\bar{1}\ 11]$ or $1/2[\bar{1}\ \bar{1}\ 1]$ dislocations and $[0\ 0\ \bar{1}]$ edge dislocations; with five examples of determination of $n = \mathbf{g}\cdot\mathbf{b}$ using the thickness fringes method.

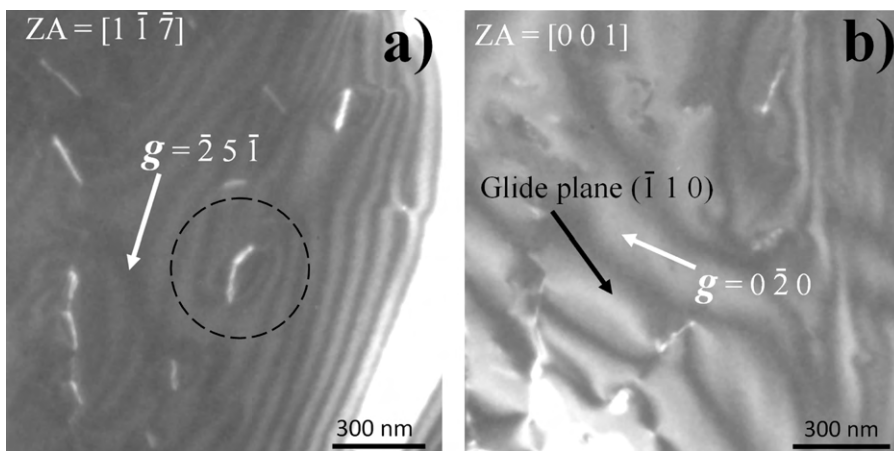


Fig. 5. WBDF images of sample 3753 showing a curved dislocation along the $[1\ \bar{1}\ \bar{7}]$ ZA, with $g = \bar{2}\ 5\ \bar{1}$ (a) and the glide plane along the $[001]$ ZA, with $g = 0\bar{2}0$ (b).

Fig. 4 shows two populations of dislocations, which exhibit different contrasts and terminating fringes:

- with $g = \bar{3}01$ (see Fig. 4a), the $\mathbf{g}\cdot\mathbf{b}$ product is $n = -1$ for dislocations with the low contrast (labelled B) and $n = 2$ for the ones with a stronger contrast (labelled A);
- with $g = 00\bar{2}$ (see Fig. 4c), the $\mathbf{g}\cdot\mathbf{b}$ product is $n = 2$ for dislocations B and $n = -1$ for dislocations A;

- then with $g = \bar{2}00$ (see Fig. 4b), the $\mathbf{g}\cdot\mathbf{b}$ product is $n = 1$ for dislocations A and dislocations B are out of contrast.

Finally, the Burgers vector of dislocations A is $1/2[\bar{1}\ 11]$ or $1/2[\bar{1}\ \bar{1}\ 1]$ and dislocations B are of the $[001]$ type. From the orientations observed in Fig. 4c, the dislocations B have an edge character. This part of the specimen contains a comparable amount of $1/2(1\ 1\ 1)$ and $[001]$ dislocations.

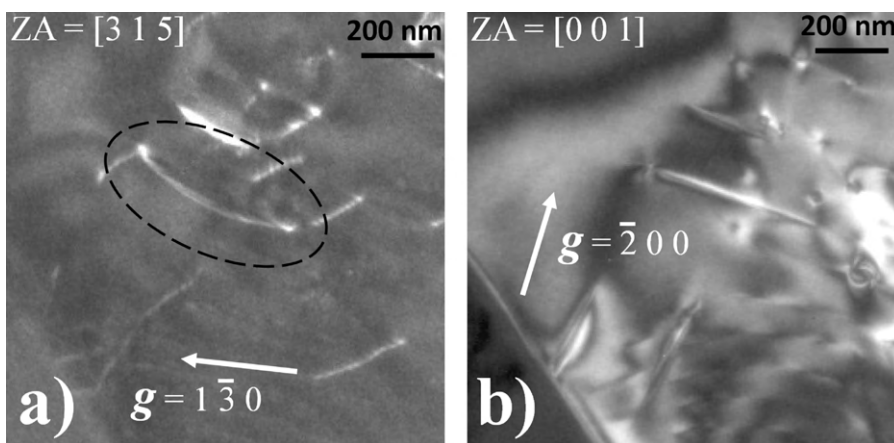


Fig. 6. WBDF images of sample 3753 showing a curved dislocation along the $[001]$ ZA, with $g = \bar{2}00$ (a) and the climb plane along the $[3\ 1\ 5]$ ZA, with $g = 1\bar{3}0$ (b).

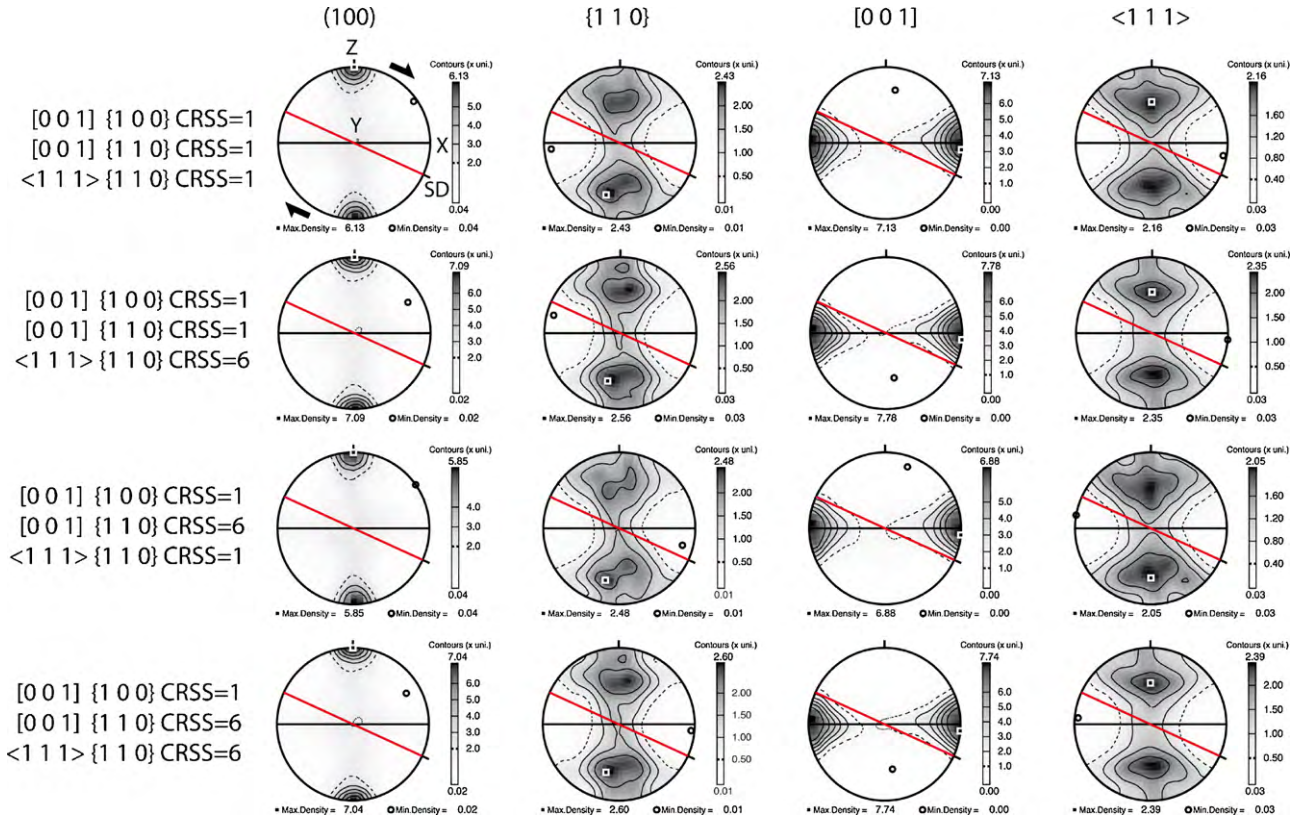


Fig. 7. Crystal preferred orientation of K-lingunite in simple shear. Model CRSS are marked on the figures. Shear strain (γ) is 1.73 (Von Mises equivalent strain of 1.0). Maximum and minimum finite strain axes are marked X and Z. The horizontal black line is the XY flattening plane or foliation. Thick black arrows mark the dextral shear sense, SD is the shear direction and the inclined red line is the shear plane. Lower hemisphere equal area projection.

Fig. 5a shows a curved dislocation segment (circled). The number of terminating fringes suggests a $\mathbf{g} \cdot \mathbf{b}$ product $n = \pm 2$ with $\mathbf{g} = 25 \bar{1}$. Considering other diffraction conditions, a Burgers vector of $\pm 1/2 [1 1 \bar{1}]$ is consistent with all images obtained for this dislocation. The specimen has been tilted until this dislocation segment appears linear. This is achieved when the area is observed along the [001] zone axis. The segment appears to lie in the ($\bar{1} 1 0$) plane (Fig. 5b). Consequently, the slip system of the curved dislocation is $1/2 [1 1 \bar{1}] (\bar{1} 1 0)$.

Fig. 6a shows another curved dislocation for which diffraction experiments give a $\pm 1/2 [\bar{1} 1 1]$ Burgers vector. Viewed along the [001] zone axis, this segment appears to lie in the (100) plane (Fig. 6b).

4.2. Visco-plastic self-consistent modelling

In order to run the VPSC models we need to define the CRSS for each slip system. The TEM analysis has shown that slip occurs on [001]{100}, the majority of the dislocations are [001] screw dislocations and these could potentially also slip on {110} and indeed on all {hk0}. However, the TEM analysis did not unambiguously identify {110} as active slip planes or effectively eliminates them either. As [001]{100} dislocations had a high density we have assigned this slip system a low relative CRSS of one. The [001]{100} system has probably a CRSS similar to [001]{110}, we have used a CRSS of one, but also of six to see how the activity of this system affects the CPO. A third slip system is observed, $1/2 \langle 1 1 1 \rangle \{1 1 0\}$, with a lower dislocation density. Without mechanical data, we have assigned a series of CRSS to this slip system between 1 and 6, assuming that it is less frequent because the shear stresses were only high enough to weakly activate the system. Four CRSS models were explored; all had the CRSS for [001]{100} equal to one, but the values for [001]{110} and $\langle 1 1 1 \rangle \{1 1 0\}$ where either one or six. The results in

Fig. 7 show for the four CRSS models that the pole figures reveal very little change in the overall distribution and only slight variations of pole figure densities.

The slip activity associated for the two CRSS models are shown in Fig. 8. The [001]{100} has a high activity (0.4–0.8) in all models. The $1/2 \langle 1 1 1 \rangle \{1 1 0\}$ slip system has moderate (0.3–0.2) activities in all models even when the CRSS equals six. The [001]{110} system has a bi-polar behaviour, if the CRSS equals one it has the same activity as [001]{100}, if the CRSS equals six, it has virtually zero activity.

4.3. Seismic properties

The high-pressure K-lingunite phase represents between 20 and 30% by volume of subducted and transformed argillaceous sediments. The anisotropic seismic properties at mantle pressures can be calculated using the CPO of K-lingunite, presented in Fig. 9, and the single crystal elastic constants and pressure derivatives recently predicted, using first-principles by Mookherjee and Steinle-Neumann (2009). The seismic properties were calculated using the numerical methods described by Mainprice (1990, 2007). The properties were calculated at a pressure of 17 GPa, the pressure of the deformation experiments, which is approximately equivalent to a depth of 500 km. At present, no temperature derivatives are available for the elastic constants. In Fig. 9, the seismic properties are illustrated using:

- the P-wave velocity (V_p) in km/s;
- anisotropy of the difference in velocity between the fastest and slowest shear wave (shear wave splitting), for a given propagation direction and (AVs) as percentage;
- and the polarization of the fastest shear wave.

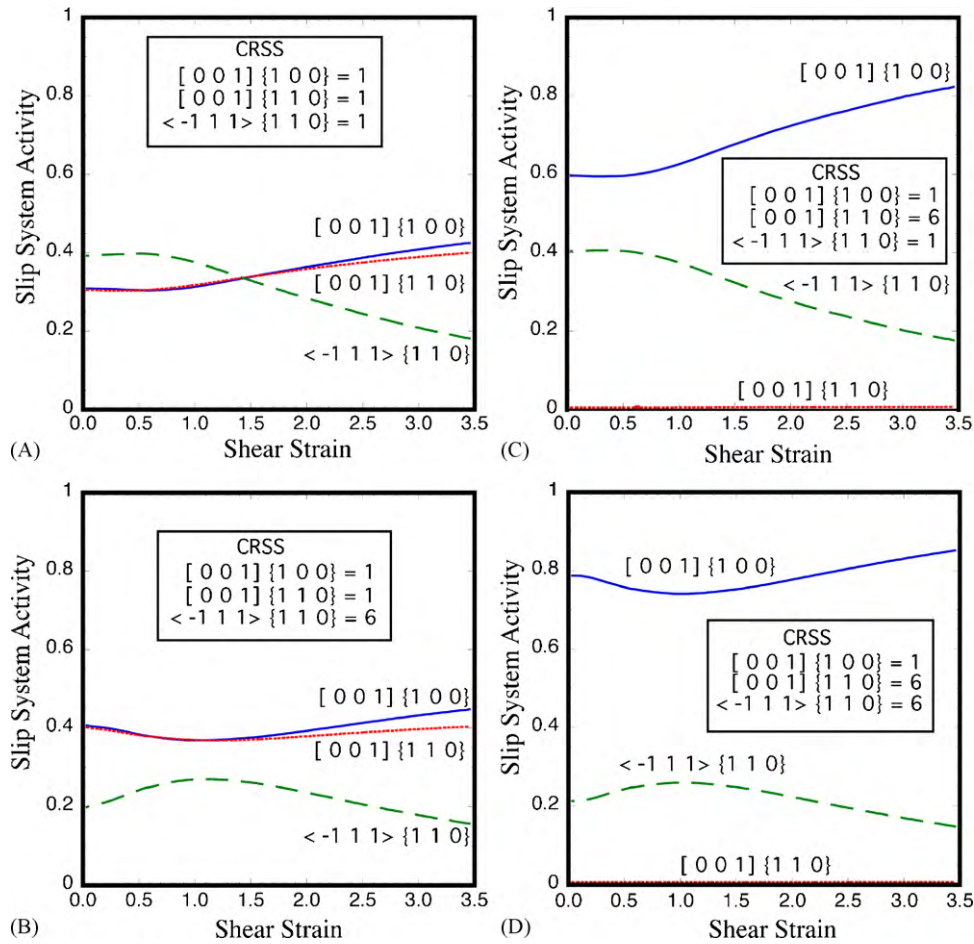


Fig. 8. Polycrystalline plastic anisotropy indicated by the slip systems activity as a function of model CRSS in simple shear with $[001]\{100\}$, $[001]\{110\}$ and $(111)\{110\}$ slip systems. Model A: all slip systems have the same CRSS, corresponding to an isotropic plastic model. Model B: this model has a CRSS of $(111)\{110\}$ six times greater than $[001]\{100\}$ and $[001]\{110\}$. Model C: it has a CRSS of $[001]\{110\}$ six times greater than $[001]\{100\}$ and $(111)\{110\}$. Model D: it has a CRSS of $[001]\{110\}$ and $(111)\{110\}$ six times greater than $[001]\{100\}$.

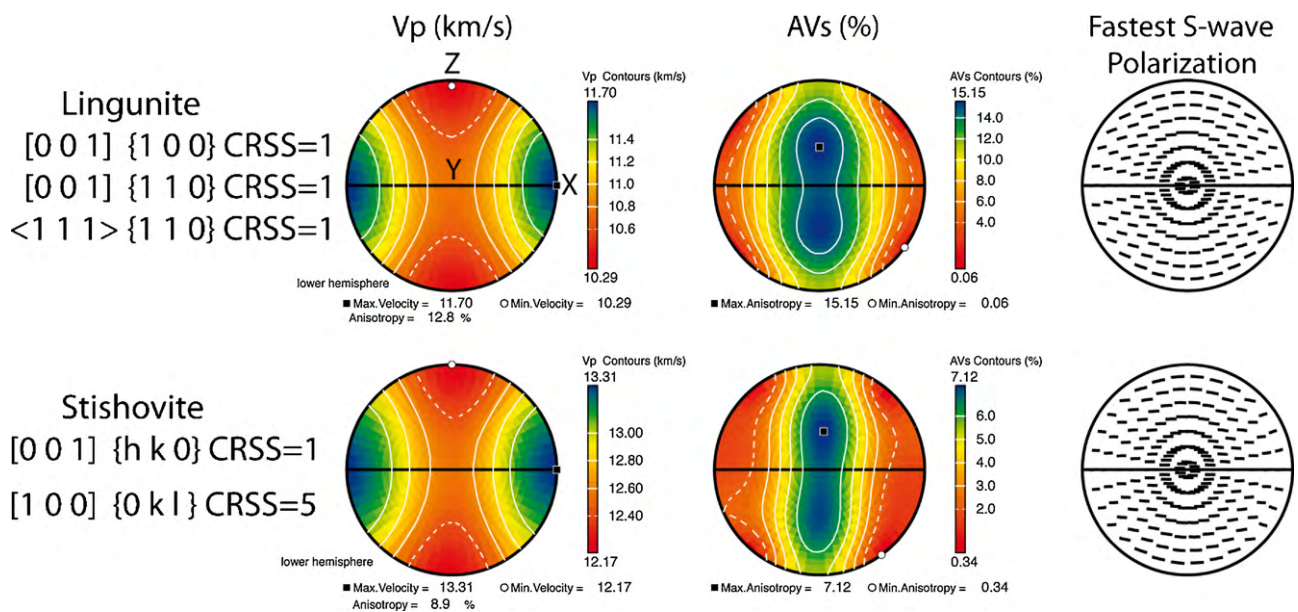


Fig. 9. The predicted seismic anisotropy at the pressure of 17 GPa, which corresponds to a 500 km depth. Above: it is composed of 100% polycrystalline K-lingunite with the CPO given in Fig. 7 at shear strain of 1.73 for the horizontal flow (XY horizontal plane). The single crystal elastic constants given by Mookherjee and Steinle-Neumann (2009) have been used. Below: it is composed of 100% polycrystalline stishovite with the CPO given in Cordier et al. (2004). Horizontal flow (XY horizontal plane). X, Y and Z are the principle finite strain axes where $X > Y > Z$. The black horizontal line is the XY plane of finite strain. Lower hemisphere equal area projection.

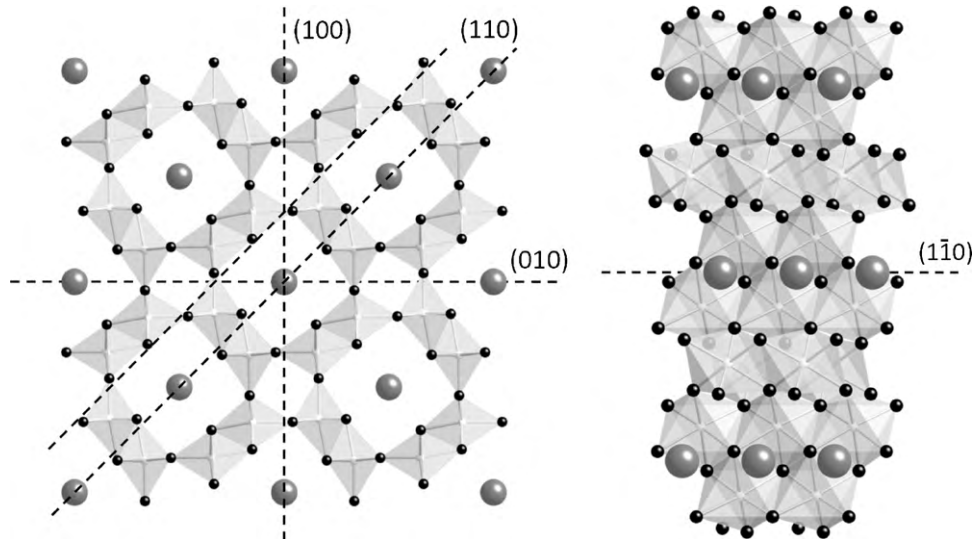


Fig. 10. Projection of the K-lingunite crystal structure along the $[001]$ direction, on the left, and along the $[111]$ direction, on the right (K is symbolized by dark grey spheres, Al octahedral and Si octahedral units are bright grey, with oxygen atom in black). The (100) , (010) , (110) and $(\bar{1}\bar{1}0)$ glide planes are represented.

The main features of the seismic anisotropy are a fast Vp velocity of 11.7 km/s parallel to X and slow Vp velocity of 10.3 km/s parallel to Z . The shear wave splitting is high in a broad region near the Y -direction, normal to X and Z and low near X . The Vp anisotropy is 12.8%, the AVs anisotropies are 15.1% for the CRSS model with all CRSS equal to one, the other models give nearly the same results. The orientation of fastest S-wave polarization is parallel to the XY plane.

5. Discussion

5.1. Slip systems and deformation mechanisms

The tetragonal cell of K-lingunite is very anisometric with $[001]$ being much smaller than $[100]$ or $[010]$ (2.723 Å to be compared with 9.315 Å). From the energetic point of view, it is expected that $[001]$ dislocations are favoured since their elastic energy (which scales with μb^2) is about ten times less than those of (100) dislocations, supposing the $\mu_{[001]\{hk0\}}$ shear modulus is nearly the same as the $\mu_{(100)\{0kl\}}$ shear modulus. Our observations support this view since the large majority of observed dislocations are of the $[001]$ type and no $[100]$ or $[010]$ dislocations could have been identified. From the crystal structure of K-lingunite, it is expected that $[001]$ dislocations can glide in $\{100\}$ or $\{110\}$. Most free $[001]$ dislocations have been shown to be of screw character rendering the identification of the slip planes difficult. The alignment of dislocations seen along the $[001]$ zone axis suggests that $[001]$ may have been activated in (010) . However, the absence of evidence of $[001]\{110\}$ glide is not sufficient to rule out the possibility of this slip system.

The body-centered lattice (I) of K-lingunite ($I4/m$) induces an additional translation vector: $1/2[111]$. With a 6.726 Å moduli, $1/2(111)$ dislocations have an elastic energy that corresponds to six times the one of $[001]$ dislocations, supposing the $\mu_{1/2(111)\{110\}}$ shear modulus is nearly the same as the $\mu_{[001]\{100\}}$ shear modulus. The activation of $1/2(111)$ glide is pervasive in our samples. The $\{110\}$ planes have been identified as possible glide planes, in agreement with crystal structure considerations (Fig. 10).

We have also observed $\pm 1/2[\bar{1}11]$ dislocations aligned along a (100) plane. Since this plane does not contain the Burgers vector, it must be considered as a climb plane. This is not the only

evidence for climb since we have observed many sub-grain boundaries in several grains (some well-organized, some less). As already pointed out in previous studies (Cordier and Rubie, 2001; Thurel and Cordier, 2003), this kind of experiments, where specimens are compressed in a non-hydrostatic environment, correspond to high stresses at the beginning of the heating, which are then relaxed. After a given (unknown) time, the stress level becomes probably very low and recovery processes are enhanced. The large number of sub-grain boundaries observed is thus not surprising. However, sub-grain formation requires climb (also shown independently with $1/2(111)$ dislocations) and hence diffusion. Our observations are thus an indication that diffusion is active in K-lingunite at 1300 °C.

5.2. Modelling CPO of K-lingunite aggregates and seismic properties

The VPSC models used the slip systems identified by TEM, namely $[001]$ glide (in $\{100\}$ and possibly in $\{110\}$) and $1/2(111)\{110\}$. The dislocation density of $[001]$ was higher and was dominated by dislocations of the screw character, which could result in “pencil” glide or cross-slip type behaviour on planes in the zone axis of the slip direction $[001]$. We assigned to this slip system the lowest CRSS of one. Simulations with all the four CRSS show that the CPO has the slip direction $[001]$ parallel to the finite strain extension X -direction, and the pole to (100) plane parallel to the finite strain shorting Z -axis. In contrast, the (111) direction and the pole to plane $\{110\}$ are oblique to Y and Z respectively. The pole figures suggest a dominant activity of $[001]$ glide, which is confirmed by the slip system activity plots. The increase in the CRSS from one to six reduces the activity of the system $1/2(111)\{110\}$ to about 20%, whereas the same increase for $[001]\{110\}$ reduces its activity to nearly zero. Reducing the activity of these glide systems is compensated by an increasing activity of $[001]\{100\}$. Pole figure densities and symmetries are virtually unaffected by these activity changes because slip in $[001]$ direction is always dominant, either on the $\{100\}$ plane or a combination of $\{100\}$ and $\{110\}$ planes, which will produce pencil-like glide configuration because of tetragonal symmetry of K-lingunite.

The seismic anisotropy calculated from the CPO for all CRSS models are also very similar, with:

- fast Vp parallel to X;
- the highest shear wave splitting anisotropy parallel to Y;
- and the fastest S-wave polarization parallel to the XY plane, plane of finite strain shortening normal to Z.

At depth of 500 km in the lower part of the transition zone, slabs are often nearly horizontal (e.g. Fukao et al., 2001; Ritsema et al., 2004; Zhao, 2004), and are very common in the circum-Pacific region. In such an idealized case, the horizontal propagation direction along X will have a high P-wave velocity and a low S-wave splitting, which would correspond to the down dip direction if the plate is slightly dipping. In contrast, the horizontal propagation direction along Y will have a moderate P-wave velocity and a high S-wave splitting with a polarization of the fastest S-wave being parallel to the horizontal plate (XY) plane. If the plate has slightly dipped, then the polarization would also have a slight inclination in relation to the horizontal. The Y-direction would correspond to the transverse direction of the plate, normal to the dip or to the subduction downward transport direction. These results can be compared with the results for stishovite VPSC models reported by Cordier et al. (2004) that we have recalculated at 17 GPa. These results show an almost identical orientation of the seismic pattern:

- high Vp parallel to X;
- high shear wave splitting parallel to Y;
- and the polarization of the fastest S-wave in the XY plane (Fig. 9).

The anisotropy of Vp and Vs are 13.3% and 7.1% respectively in stishovite. These data can be compared with 12.8% and 15.1% for K-lingunite. Stishovite has a volume fraction of 25% at the transition zone depth ranges. Clearly, the anisotropy of K-lingunite and stishovite would constructively combine giving an effective volume fraction of about 50% of the transformed sediments. The other phases present are majorite (30%), clinopyroxene (5%) and CaAlSi-phase (15%) (Irifune et al., 1994). Of these phases, only majorite is volumetrically important. The pure Mg end-member majorite of the majorite–pyrope garnet solid solution has tetragonal symmetry and is relatively weakly anisotropic with 1.8% for Vp and 9.1% for Vs (Pacalo and Weidner, 1997; Sinogeikin and Bass, 2002a,b). Naturally deformed garnets do not have strong CPOs in eclogites (Mainprice et al., 2004). Nothing is known about majorite CPO, but they are probably similar to the weak CPO of garnets and hence polycrystalline majorite will have isotropic seismic properties. It seems likely that the anisotropic seismic properties of subducted and transformed sediments will be dominated by the combined 50% volume fraction of anisotropic K-lingunite and stishovite.

Global studies of radial seismic anisotropy of the deep mantle have shown that in the transition zone (400–700 km depth), regions of subducted slab material are associated with $V_{sv} > V_{sh}$ (e.g. Panning and Romanowicz, 2006; Visser et al., 2008). These global studies would probably not detect the anisotropy associated with a thin veneer of transformed sediments on the slab upper surface. If the anisotropy combined of the K-lingunite and stishovite contributes to the observation of the $V_{sv} > V_{sh}$ signal, then the slab would have an inclination of 45° or more. This aspect seems unlikely for regions with horizontal slabs in the transition zone. However, regional studies of horizontal propagation paths in the mid mantle show that the fastest S-waves are polarized horizontally ($V_{sh} > V_{sv}$) (e.g. Chen and Brudzinski, 2003; Wookey et al., 2002; Wookey and Kendall, 2004). In this case the anisotropy of K-lingunite and stishovite could contribute to this signal, especially if the transformed sediment acted as a wave-guide.

6. Conclusion

The plastic deformation mechanisms of K-lingunite are strongly controlled by the plate-shaped crystal structure. The very anisometric tetragonal unit cell strongly favours [001] slip. Most of the dislocations are [001] screws, which makes the determination of glide planes difficult. A secondary slip in $1/2(111)\{110\}$ has also been characterized with a low occurrence rate. Using the observed glide systems and VPSC model, the CPO of K-lingunite aggregates has been obtained. The texture of polycrystalline K-lingunite shows that the slip direction [001] is parallel to the slab strain X-direction and the pole to (100) plane is parallel to the slab strain Z axis. On the contrary, the $\langle 111 \rangle$ direction and the pole to $\{110\}$ plane are tilted from the Y and the Z slab axes respectively. The seismic properties of K-lingunite aggregates at 17 GPa were calculated according to these CPO and to the single crystal elasticity tensor. Considering that the subducted slab is only composed of K-lingunite, then:

The P-waves are faster in parallel with the finite extending X-direction (maximal Vp = 11.7 km/s) and are slower in parallel with the finite shorting Z-direction (minimal Vp = 10.3 km/s);

The S-wave anisotropy is characterized by a high shear wave splitting (15.1%) in the finite flattening (XY) plane in the Y-direction. The fastest S-waves have their polarization directions in the XY plane.

Actually, K-lingunite is 25% by volume of the subducted and transformed argillaceous sediments. The other phases present are stishovite (25%), majorite (30%), CaAlSi-phase (15%) and clinopyroxene (5%). It is expected that majorite has a weak CPO and a weak crystal anisotropy. The seismic anisotropy of the CaAlSi-phase and clinopyroxene phases can be neglected due to their small proportion. Only stishovite is likely to have a strong CPO and a strong single crystal anisotropy. Indeed, stishovite has roughly the same polycrystalline seismic anisotropy pattern than the K-lingunite one, which would combine constructively. Even if the transformed sediments correspond to a thin crustal layer of a thickness of few kilometres, they could act as an anisotropic wave-guide for seismic waves propagating through the slab surface. At a 500 km depth, corresponding to the 17 GPa of the experiments, slabs are often horizontal; hence horizontally propagating seismic waves could sample the transformed sediment anisotropy over long distances.

Acknowledgements

We thank H. Schulze for his support of preparation of the thin sections of the recovered samples. The TEM national facility in Lille is supported by the CNRS (INSU) and the Conseil Régional du Nord – Pas de Calais, France.

References

- Chastel, Y.B., Dawson, P.R., Wenk, H.R., Bennett, K., 1993. Anisotropic convection with implications for the upper mantle. *J. Geophys. Res.* 98, 17757–17771, doi:10.1029/93JB01161.
- Chen, W.P., Brudzinski, M.R., 2003. Seismic anisotropy in the mantle transition zone beneath Fiji-Tonga. *Geophys. Res. Lett.* 30, 15.1–15.4, doi:10.1029/2002GL016330.
- Cordier, P., Rubie, D.C., 2001. Plastic deformation of minerals under extreme pressure using a multi-anvil apparatus. *Mater. Sci. Eng. A* 309–310, 38–43, doi:10.1016/S0921-5093(00)01795-0.
- Cordier, P., Mainprice, D., Mosenfelder, J.L., 2004. Mechanical instability near the stishovite–CaCl₂ phase transition: implications for crystal preferred orientations and seismic properties. *Eur. J. Miner.* 16, 387–399, doi:10.1127/0935-1221/2004/0016-0387.
- Eshelby, J.D., 1957. The determination of the elastic field of an ellipsoidal inclusion, and related problems. *Proc. R. Soc. London* 241, 376–396.
- Irifune, T., Ringwood, A.E., Hibberson, W.O., 1994. Subduction of continental crust and terrigenous and pelagic sediments: an experimental study. *Earth Planet. Sci. Lett.* 126, 351–368, doi:10.1016/0012-821X(94)90117-1.

- Ferroir, T., Onozawa, T., Yagi, T., Merkel, S., Miyajima, N., Nishiyama, N., Irifune, T., Kikegawa, T., 2006. Equation of state and phase transition in K-hollandite at high pressure. *Am. Miner.* 91, 327–332, doi:10.2138/am.2006.1879.
- Fukao, Y., Widiyantoro, S., Obayashi, M., 2001. Stagnant slabs in the upper and lower mantle transition region. *Rev. Geophys.* 39, 291–323.
- Gillet, P., Chen, M., Dubrovinsky, L., El Goresy, A., 2000. Natural NaAlSi₃O₈-hollandite in the shocked sixiangkou meteorite. *Nature* 287, 1633–1636, doi:10.1126/science.287.5458.1633.
- Ham, R.K., 1961. The determination of dislocation densities in thin films. *Phil. Mag.* 6, 1183–1184, doi:10.1080/14786436108239679.
- Ishida, Y., Ishida, H., Kohra, K., Ichinose, H., 1980. Determination of the Burgers vector of a dislocation by weak-beam imaging in a HVEM. *Phil. Mag. A* 42, 453–462, doi:10.1080/01418618008239369.
- Langenhorst, F., Dressler, B., 2003. First observation of silicate hollandite in a terrestrial rock. In: *Proceeding of the Third International Conference on Large Meteorite Impacts Geological Society of America Special Paper, Abstract-#4046*.
- Langenhorst, F., Poirier, J.P., 2000a. Anatomy of black veins in Zagami: clues to the formation of high-pressure phases. *Earth Planet. Sci. Lett.* 184, 37–55, doi:10.1016/S0012-821X(00)00317-4.
- Langenhorst, F., Poirier, J.P., 2000b. 'Eclogitic' minerals in a shocked basaltic meteorite. *Earth Planet. Sci. Lett.* 176, 259–265, doi:10.1016/S0012-821X(00)00028-5.
- Lebensohn, R.A., Tomé, C.N., 1993. A self-consistent anisotropic approach for the simulation of plastic deformation and texture development of polycrystals: application to zirconium alloys. *Acta Met. Mater.* 41, 2611–2624, doi:10.1016/0956-7151(93)90130-K.
- Liu, L.G., El Goresy, A., 2007. High-pressure phase transitions of the feldspars and further characterization of lingunite. *Inter. Geol. Rev.* 49, 854–860, doi:10.2747/0020-6814.49.9.854.
- Mainprice, D., 1990. An efficient FORTRAN program to calculate seismic anisotropy from the lattice preferred orientation of minerals. *Comput. Geosci.* 16, 385–393.
- Mainprice, D., 2007. Seismic anisotropy of the deep Earth from a mineral and rock physics perspective. *Treatise in Geophysics*. In: Schubert, G. (Editor-in-Chief), vol. 2 Mineral Physics, In: Price, G.D. (Ed.). Elsevier, Oxford, pp. 437–492.
- Mainprice, D., Bascou, J., Cordier, P., Tommasi, A., 2004. Crystal preferred orientations of garnet: comparisons of numerical simulations with naturally deformed Eclogites. *J. Struct. Geol.* 26, 2089–2102.
- Miyajima, N., Walte, N., 2009. Burgers vector determination in deformed perovskite and post-perovskite of CaIrO₃ using thickness fringes in weak-beam dark-field images. *Ultramicroscopy* 109, 683–692, doi:10.1016/j.ultramic.2009.01.010.
- Molinari, A., Canova, G.R., Azhy, S., 1987. A self-consistent approach of the large deformation crystal polycrystal viscoplasticity. *Acta Metall.* 35, 2983–2994, doi:10.1016/0001-6160(87)90297-5.
- Mookherjee, M., Steinle-Neumann, G., 2009. Detecting deeply subducted crust from the elasticity of hollandite. *Earth Planet. Sci. Lett.* 288, 349–358, doi:10.1016/j.epsl.2009.09.037.
- Morniroli, J.P., Ji, G., 2009. Identification of the kinematical forbidden reflections from precession electron diffraction. *Mater. Res. Soc. Symp. Proc.*, doi:10.1557/PROC-1184-GG01-03, 1184-GG01-03.
- Nishiyama, N., Rapp, R.P., Irifune, T., Sanehira, T., Yamazaki, D., Funakoshi, K., 2005. Stability and *P–V–T* equation of state of KAlSi₃O₈-hollandite determined by in situ X-ray observations and implications for dynamics of subducted continental crust material. *Phys. Chem. Miner.* 32, 627–637, doi:10.1007/s00269-005-0037-y.
- Pacalo, R.E.G., Weidner, D.J., 1997. Elasticity of majorite, MgSiO₃ tetragonal garnet. *Phys. Earth Planet. Inter.* 99, 145–154, doi:10.1016/S0031-9201(96)03158-5.
- Panning, M., Romanowicz, B., 2006. Three-dimensional radially anisotropic model of shear velocity in the whole mantle. *Geophys. J. Int.* 167, 361–379, doi:10.1111/j.1365-246X.2006.03100.x.
- Ritsema, J., van Heijst, H.-J., Woodhouse, J.H., 2004. Global transition zone tomography. *J. Geophys. Res.* 109, B02302, doi:10.1029/2003JB002610.
- Ringwood, A.E., Reid, A.F., Wadsley, A.D., 1967. High-pressure KAlSi₃O₈, an aluminosilicate with sixfold coordination. *Acta Cryst.* 23, 1093–1095, doi:10.1107/S0365110X6700430X.
- Sinogeikin, S.V., Bass, J.D., 2002a. Elasticity of majorite and a majorite–pyrope solid solution to high pressure; implications for the transition zone. *Geophys. Res. Lett.* 29, 4.1–4.4, doi:10.1029/2001GL013937.
- Sinogeikin, S.V., Bass, J.D., 2002b. Elasticity of pyrope and majorite–pyrope solid solutions to high temperatures. *Earth Planet. Sci. Lett.* 203, 549–555, doi:10.1016/S0012-821X(02)00851-8.
- Taylor, G.I., 1938. Plastic strain in metals. *J. Inst. Met.* 62, 307–324.
- Thurel, E., Cordier, P., 2003. Plastic deformation of wadsleyite. I. High-pressure deformation in compression. *Phys. Chem. Miner.* 30, 256–266, doi:10.1007/s00269-003-0312-8.
- Tomé, C.N., Lebensohn, R., 2004. Self consistent homogenization methods for texture and anisotropy. In: Raabe, D., Roters, F., Barlat, F., Chen, L.-Q. (Eds.), *Continuum Scale Simulation of Engineering Materials: Fundamentals – Microstructures – Process Applications*. J. Wiley & Sons, NY, ISBN 3-527-30760-5, pp. 462–489.
- Tomioka, N., Mori, H., Fujino, K., 2000. Shock-induced transition of NaAlSi₃O₈. Feldspar into a hollandite structure in a L6 chondrite. *Geophys. Res. Lett.* 27, 3397–4000, doi:10.1029/2000GL008513.
- Tommasi, A., Mainprice, D., Canova, G., Chastel, Y., 2000. Viscoplastic self-consistent and equilibrium-based modeling of olivine lattice preferred orientations. Implications for upper mantle seismic anisotropy. *J. Geophys. Res.* 105, 7893–7908.
- Tommasi, A., Mainprice, D., Cordier, P., Thoraval, C., Couvy, H., 2004. Strain-induced seismic anisotropy of wadsleyite polycrystals and flow patterns in the mantle transition zone. *J. Geophys. Res.* 109, B12405, doi:10.1029/2004JB003158.
- Urakawa, S., Kondo, T., Igawa, N., Shimomura, O., Ohno, H., 1994. Synchrotron radiation study on the high-pressure and high-temperature phase relations of KAlSi₃O₈. *Phys. Chem. Miner.* 21, 387–391, doi:10.1007/BF00203296.
- Vincent, R., Midgley, P.A., 1994. Double conical beam-rocking system for measurement of integrated electron diffraction intensities. *Ultramicroscopy* 53, 271–282, doi:10.1016/0304-3991(94)90039-6.
- Wenk, H.-R., Bennett, K., Canova, G.R., Molinari, A., 1991. Modelling plastic deformation of peridotite with the self-consistent theory. *J. Geophys. Res.* 96, 8337–8349.
- Visser, K., Trampert, J., Lebedev, S., Kennett, B.L.N., 2008. Probability of radial anisotropy in the deep mantle. *Earth Planet. Sci. Lett.* 270, 241–250, doi:10.1016/j.epsl.2008.03.041.
- Wookey, J., Kendall, J.-M., Barruol, G., 2002. Mid-mantle deformation inferred from seismic anisotropy. *Nature* 415, 777–780, doi:10.1038/415777a.
- Wookey, J., Kendall, J.-M., 2004. Evidence of midmantle anisotropy from shear wave splitting and the influence of shear-coupled P waves. *J. Geophys. Res.* 109, B07309, doi:10.1029/2003JB002871.
- Xie, X., Chen, M., Wang, D., El Goresy, A., 2001. NaAlSi₃O₈-hollandite and other high-pressure minerals in the shock melt veins of the Suizhou meteorite. *Chin. Sci. Bull.* 46, 1121–1126, doi:10.1007/BF02900692.
- Yagi, A., Suzuki, T., Akaogi, M., 1994. High pressure transitions in the system KAlSi₃O₈-NaAlSi₃O₈. *Phys. Chem. Miner.* 21, 12, doi:10.1007/BF00205210.
- Zhang, J., Ko, J., Hazen, R.M., Prewitt, C.T., 1993. High-pressure crystal chemistry of KAlSi₃O₈ hollandite. *Am. Miner.* 78, 493–499.
- Zhao, D., 2004. Global tomographic images of mantle plumes and subducting slabs: insight into deep Earth dynamics. *Phys. Earth Planet. Inter.* 146, 3–34, doi:10.1016/j.pepi.2003.07.032.